# Supplementary Information: Far-field extraction of the dielectric function of exfoliated flakes near phonon resonances.

Mitradeep Sarkar, Michael T. Enders, Mehrdad Shokooh-Saremi, Evgenia Klironomou, Gonzalo Álvarez-Pérez, Kenji Watanabe, Takashi Taniguchi, Hanan H. Sheinfux, Frank H.L Koppens, Georgia T. Papadakis

## Contents

# 1 The analytical expressions for reflectance from the material.

## 1.1 Reflectance measured by the Cassegrain objective.

The system consists of an incident medium with permittivity $\epsilon_1 = n_1^2 = 1$, a substrate with $\aleph_S = (n_S + ik_S)$ and a thin layer of thickness $d$ with permittivity $\epsilon$. The material is considered to be anisotropic with diagonal complex permittivities $\epsilon_X$, $\epsilon_Y = \epsilon_x/\alpha_Y^2$, and $\epsilon_Z = \epsilon_x/\alpha_Z^2$. The reflection ($r_{p/s}$) and transmission ($t_{p/s}$) of the system can be written in terms of the transfer matrices as

$$\begin{bmatrix} t_s \\ t_p \\ 0 \\ 0 \end{bmatrix} = K_2^{-1} M K_1 \begin{bmatrix} a_s \\ a_p \\ r_s \\ r_p \end{bmatrix} \tag{S1}$$

where $a_s$ and $a_p$ are the TE and TM polarized incident fields. $K_2$ and $K_1$ are the boundary conditions for material-substrate and material-incident medium interfaces respectively.

$$K_{2/1} = \begin{bmatrix} 0 & -cos\theta & 0 & cos\theta \\ 1 & 0 & 1 & 0 \\ -\frac{\sqrt{\epsilon_{2/1}}}{\eta_0} cos\theta & 0 & \frac{\sqrt{\epsilon_{2/1}}}{\eta_0} cos\theta & 0 \\ 0 & -\frac{\sqrt{\epsilon_{2/1}}}{\eta_0} & 0 & -\frac{\sqrt{\epsilon_{2/1}}}{\eta_0} \end{bmatrix} \tag{S2}$$

with $\eta_0 = \sqrt{\mu_0/\epsilon_0}$. The transfer matrix for the material can be written as $M = e^{iPh}$, with

$$P = \omega \begin{bmatrix} 0 & 0 & 0 & \eta_0^2 - \eta_0^2 sin^2\theta/\epsilon_Z \\ 0 & 0 & -\eta_0^2 & 0 \\ 0 & -\epsilon_Y + sin^2\theta & 0 & 0 \\ \epsilon_X & 0 & 0 & 0 \end{bmatrix} \tag{S3}$$

After matrix exponential, $M$ can be written as

$$\begin{bmatrix} cos(k_0 d\aleph_X) & 0 & 0 & i\frac{\eta_0 \aleph_X sin(k_0 d\aleph_X)}{\epsilon_x} \\ 0 & cos(k_0 d\aleph_Y) & -i\frac{\eta_0 sin(k_0 d\aleph_Y)}{\aleph_Y} & 0 \\ 0 & -i\frac{\aleph_Y sin(k_0 d\aleph_Y)}{\eta_0} & cos(k_0 d\aleph_Y) & 0 \\ i\frac{\epsilon_X sin(k_0 d\aleph_X)}{\eta_0 \aleph_X} & 0 & 0 & cos(k_0 d\aleph_X) \end{bmatrix} \tag{S4}$$

Performing the matrix multiplication and rearranging the terms, for $n_1 = 1$ and $n_2 = \aleph_S$, one can derive the following explicit relations for the reflectance for P and S polarizations

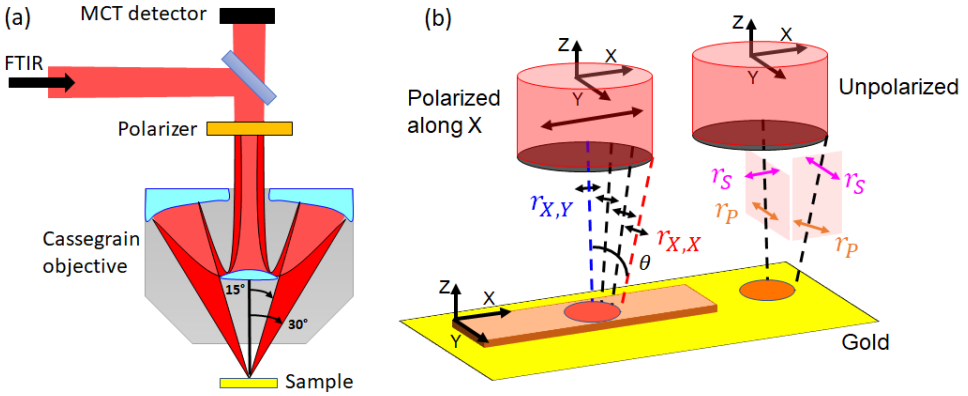


**Fig. S1** (a) Schematic of the FTIR microscope setup used for the reflectance spectra measurements. The angular range of the Cassegrain objective is shown. (b) The schematic representation of a beam polarized along $X$, focused at a spot. The reflectance from the spot can be decomposed in two orthogonal directions $X$ and $Y$, shown as red and blue in the schematic. The electric field orientation for the two directions is also shown. Also the conventional orientations of the electric field for P and S polarizations when the incident plane is along $X$ or $Y$ is demonstrated in the figure.

$$
\begin{aligned}
r_P &= \frac{\left[1-\frac{cos\theta_T}{\aleph_S cos\theta}\right]+i\left[\frac{\aleph_X}{\epsilon_X 2cos\theta}-\frac{\epsilon_X cos\theta_T}{\aleph_S \aleph_X}\right]tan(dk_0\aleph_X)}{\left[1+\frac{cos\theta_T}{\aleph_S cos\theta}\right]-i\left[\frac{n_1\aleph_X}{\epsilon_X cos\theta}+\frac{\epsilon_X cos\theta_T}{\aleph_S \aleph_X}\right]tan(dk_0\aleph_X)} \\
r_S &= \frac{\left[\frac{cos\theta}{\aleph_S cos\theta_T}-1\right]+i\left[\frac{\aleph_Y}{\aleph_S cos\theta_T}-\frac{cos\theta}{\aleph_Y}\right]tan(dk_0\aleph_Y)}{\left[\frac{cos\theta}{\aleph_S cos\theta_T}+1\right]-i\left[\frac{\aleph_Y}{\aleph_S cos\theta_T}+\frac{cos\theta}{\aleph_Y}\right]tan(dk_0\aleph_Y)}
\end{aligned}
\tag{S5}
$$

where $\aleph_X = \sqrt{\epsilon_X - \alpha_Z^2 sin^2\theta}$ and $\aleph_Y = \sqrt{\epsilon_Y - sin^2\theta}$ are the effective indices of the anisotropic material along $X$ and $Y$ axes respectively. The plane of incidence is considered along $X$ and the angle of incidence is $\theta$ with $sin\,(\theta) = \aleph_S sin\,(\theta_T)$.

Fig. S1, shows the schematic of the Cassegrain objective used for the reflectance measurements. A beam of light focused by such an objective and the electric field orientations when the incident light is polarized along $X$ is shown in Fig. S1b. The reflectance measured in this case can be decomposed into two orthogonal planes along $XZ$ and $YZ$. The electric field orientation for the light incident along the $XZ$ plane is same as P-polarized light in the $XZ$ plane of incidence. So $r_{X,X} = r_P$ of Eq. S5. However, for $r_{X,Y}$, we need to consider the expression for $r_S$ when $YZ$ is the plane of incidence. This can be obtained by replacing the $\epsilon_Y$ of Eq. S5 by $\epsilon_X$. Hence the term $\aleph_Y$ should be replaced by $\aleph_X = \sqrt{\epsilon_X - sin^2\theta}$. So the analytical expressions for the reflectance using the Cassegrain objective is given as $R_X = (r_{X,X}r^*_{X,X} + r_{X,Y}r^*_{X,Y})/2$ where

$$r_{X,X} = \frac{\left(1 - \frac{cos(\theta_T)}{\aleph_S cos(\theta)}\right) + i\left(\frac{\aleph_X}{\epsilon_X cos(\theta)} - \frac{\epsilon_X cos(\theta_T)}{\aleph_S \aleph_X}\right) tan(dk_0\aleph_X)}{\left(1 + \frac{cos(\theta_T)}{\aleph_S cos(\theta)}\right) - i\left(\frac{\aleph_X}{\epsilon_X cos(\theta)} + \frac{\epsilon_X cos(\theta_T)}{\aleph_S \aleph_X}\right) tan(dk_0\aleph_X)}$$
$$r_{X,Y} = \frac{\left(\frac{cos(\theta)}{\aleph_S cos(\theta_T)} - 1\right) + i\left(\frac{\aleph_X}{\aleph_S cos(\theta_T)} - \frac{cos(\theta)}{\aleph_X}\right) tan(dk_0\aleph_X)}{\left(\frac{cos(\theta)}{\aleph_S cos(\theta_T)} + 1\right) - i\left(\frac{\aleph_X}{\aleph_S cos(\theta_T)} + \frac{cos(\theta)}{\aleph_X}\right) tan(dk_0\aleph_X)} \tag{S6}$$

This is shown in the main article (Eq. 3) for $\theta = \theta_T = 0$. We note that the $\theta$ dependence in Eq. S10 comes from the term $\aleph_X = \sqrt{\epsilon_X - sin^2\theta}$. For the FTIR microscope used, the central angle of incidence is $\theta \approx 22°$. For vdW materials, near the Reststrahlen band, $|\epsilon_X| \gg sin^2\theta$, hence we can consider normal incidence for the analytical expressions.

## 1.2 Reflection coefficient for incident light polarized at an angle Ψ to the X-axis.

We consider an in-plane anisotropic material with effective refractive indices $\aleph_X$ and $\aleph_Y$ along X and Y. The reflection matrix in (X,Y) basis can be written as

$$R_{XY} = \begin{bmatrix} r_X & 0 \\ 0 & r_Y \end{bmatrix} \tag{S7}$$

The reflection matrix in (S,P) basis for incident light polarized at an angle Ψ to X is written as

$$R_{SP} = \mathbb{R}(\Psi) R_{XY} \mathbb{R}^{-1}(\Psi) = \begin{bmatrix} r_{SS} & r_{SP} \\ r_{PS} & r_{PP} \end{bmatrix} \tag{S8}$$

where the $\mathbb{R}$ is the rotation matrix given as

$$\mathbb{R}(\Psi) = \begin{bmatrix} \cos(\Psi) & -\sin(\Psi) \\ \sin(\Psi) & \cos(\Psi) \end{bmatrix} \tag{S9}$$

From Eq. S8 we get

$$\begin{aligned} r_{SS} &= \cos^2(\Psi) r_X + \sin^2(\Psi) r_Y \\ r_{PP} &= \sin^2(\Psi) r_X + \cos^2(\Psi) r_Y \\ r_{SP} = r_{PS} &= \cos(\Psi)\sin(\Psi)(r_Y - r_X) \end{aligned} \tag{S10}$$

For $\Psi = 45°$ we get

$$r_{SS} = r_{PP} = \frac{r_X + r_Y}{2} \tag{S11}$$

This is used in the main article (Eq. 5) to estimate $k_X$ with known values of $n_Y$ and $k_Y$.

# 2 Experimental Methods.

## 2.1 Experimental discrepancies in the measurement of reflectance spectra.

A typical exfoliated flake of hBN on a gold substrate is shown in Fig. S2a. The cross-sectional area of such flakes is roughly $\sim 50\,\mu\text{m} \times 50\,\mu\text{m}$. We also see that the thickness ($d$) of the flake is not uniform over the entire surface of the flake. The thicknesses used in this work were measured using Atomic Force Microscopy (AFM). A thickness profile on the hBN flake is shown in Fig. S2b. Two distinct height distributions at $d = 95\text{nm}$ and $d = 275\text{nm}$ were observed for this particular flake.

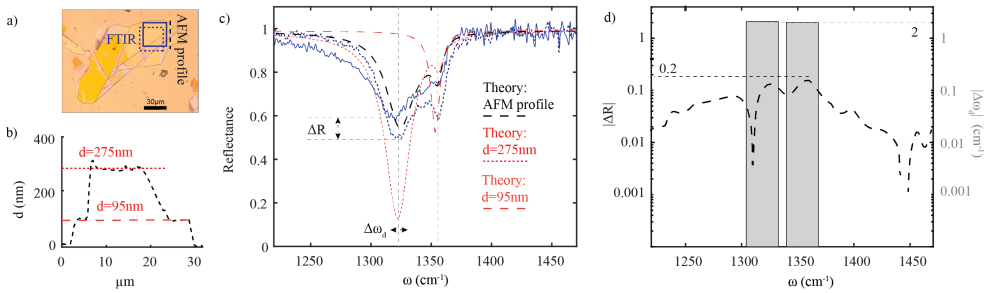


**Fig. S2** (a) Microscope image of an hBN flake on gold. (b) Flake thickness $d$ obtained by AFM along the black dashed line shown in (a). Two distinct thicknesses are observed shown by dashed red lines. (c) The reflectance spectrum was obtained by FTIR microscopy on two different locations of the flake (blue lines). The regions are marked in (a) using the same blue lines. The theoretical reflectance spectra are shown by dashed red lines for $d = 275\,\text{nm}$, $d = 95\,\text{nm}$ and for the thickness profile shown in (b) (black dashed). (d) The difference in reflectance ($|\Delta R|$) as a function of frequency for the two FTIR spectra of (c) (left axis). The maximum $|\Delta R|$ over the measured spectral range is 0.2. The frequency difference ($|\Delta\omega_\text{d}|$) of the reflectance minima for the same two FTIR spectra (right axis). $|\Delta\omega_\text{d}|$ for the two reflectance minima is $2\,\text{cm}^{-1}$.

A standard reflectance spectrum, obtained via FTIR is shown in Fig. S2c, taken on two different locations of the flake. There is a high reflectance dispersion ($|\Delta R|$) due to the non-uniformity of the flake, which is a typical discrepancy for far-field measurements in exfoliated vdW flakes. Furthermore, as the lateral dimensions of the exfoliated flakes are comparable to the wavelength of MLIR light, it results in significant diffraction and boundary effects.

The reflectance from an hBN film of a given thickness, on a gold substrate is calculated by Eq. S12 and the spectra are plotted together on Fig. S2c for $d = 95\,\text{nm}$ and $d = 275\,\text{nm}$ (red dashed). The theoretical $R$ corresponding to the experimental flake's height variation (Fig. S2b) is also shown (black dashed). The permittivity of hBN retrieved by the method presented in this article was used for these calculations. We see that none of the theoretical spectra closely resembles the experimental curves.

Hence, any attempt to retrieve the optical permittivity of hBN by fitting the experimental reflectance spectra to theoretical calculations is expected to result in large errors.

However, the spectral positions of the dips in reflectance ($\omega_\mathrm{d}$), caused by FP resonances, show statistically much less variation with sample location, as seen in Fig. S2c. The two dips observed in the reflectance spectra correspond closely to hBN thicknesses of $d = 95\,\mathrm{nm}$ and $d = 275\,\mathrm{nm}$. The maximum experimental discrepancy in reflectance ($|\Delta R|$) was found to be 0.2 whereas that for $|\Delta\omega_\mathrm{d}| = 2\,\mathrm{cm}^{-1}$ for both the reflectance dips (Fig. S2d). Therefore, retrieval of optical permittivity based on $\omega_\mathrm{d}$ rather than fitting to the entire reflectance spectrum is more robust and precise. This is further demonstrated for other hBN flakes and $\alpha$-$MoO_3$ below.

In Fig. S3 we show that even with negligible height dispersions, the experimental spectra do not match the analytically calculated spectra, more so for larger frequencies. This discrepancy is observed for the absolute value of the reflectance, while the positions of the reflectance dips closely follow the theoretically calculated $\omega_d$. Hence, the complex permittivity of hBN, obtained by fitting theoretical reflectance spectra to the measured spectra will not be accurate. This result further confirms the necessity of our method to extract the complex permittivity from micrometric flakes. The following 11 flakes and the corresponding values of $\omega_d$ were used to extract the complex permittivity of hBN.

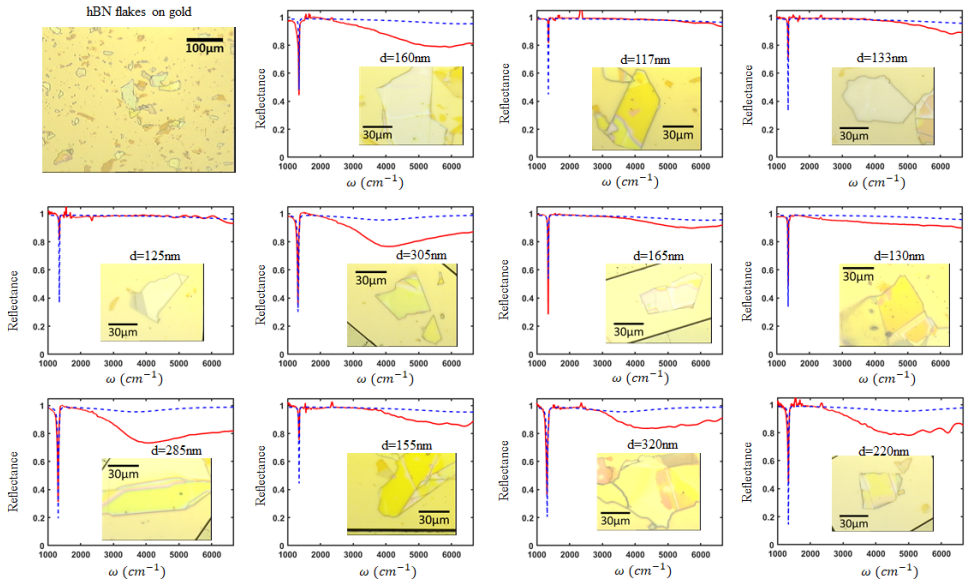


**Fig. S3** Microscope image of hBN flakes of different heights (d) on a gold substrate. The experimental reflectance spectra (red) for each flake as obtained by the FTIR is shown. The microscope images of the corresponding flakes is shown as inset along with the thickness of the flake as measured by AFM. The analytically calculated reflectance spectra is shown as blue dashed lines. The permittivity of hBN derived during this work was used for the theoretical calculations.

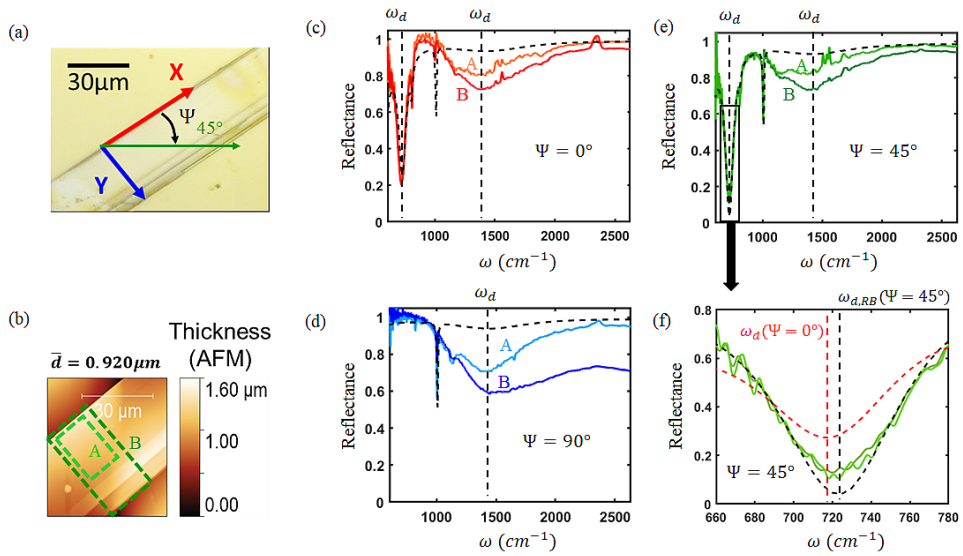


**Fig. S4** (a) Microscope image of $\alpha$-$MoO_3$ flake on a gold substrate. (b) The thickness of the flake as measured by AFM. The average thickness of the flake was 920 nm. (c) The experimental reflectance spectra of the flake with incident polarization along $X$, measured at two different locations of the flake. The two measured areas are shown in (b) and marked as A and B. (d) The same as (c) for incident polarization along $Y$. (e) The same for incident polarization at 45° to the $X$ axis. (f) The reflectance spectra around the resonance frequency $\omega_d < \omega_{\mathrm{TO}}$. The analytical reflectance spectra using the permittivity values of $\alpha$-$MoO_3$ obtained by our method is shown as black dashed lines in (c), (d), (e) and (f). The dashed red curve in f represents the analytical reflectance when the incident light is polarized along $X$.

The experimental discrepancy for $\alpha$-$MoO_3$ is shown in Fig. S4. The reflectance spectra were measured at two different areas on the same flake as shown in Fig. S4b. The reflectance spectra with the incident light polarized along $X$, $Y$, and at 45° to $X$ are shown in the figure. We see that as for hBN, the positions of the reflectance dips do not change significantly between the two measurements, however, the absolute value of the reflectance has significant variations, mainly for higher frequencies.

The analytical reflectance spectra using the permittivity values obtained by our method is also shown in Fig. S4. We see that for all the cases, the analytical reflectance spectra deviates from the measured reflectance spectra in terms of absolute value, but follows closely the positions of the reflectance dips. This further validates our method which is based on the identification of the positions of the reflectance dips, rather than fitting the theoretical reflectance spectra to the measured spectra.

## 2.2 Extracting the refractive index from reflectance dip positions.

The reflectance for normal incidence from Eq. S10 is given as

$$r_{\mathrm{X}} = \frac{\left(1 - \frac{1}{\aleph_{\mathrm{S}}}\right) + i\left(\frac{1}{\aleph_{\mathrm{X}}} - \frac{\aleph_{\mathrm{X}}}{\aleph_{\mathrm{S}}}\right) T_{\mathrm{eX}}}{\left(1 + \frac{1}{\aleph_{\mathrm{S}}}\right) - i\left(\frac{1}{\aleph_{\mathrm{X}}} + \frac{\aleph_{\mathrm{X}}}{\aleph_{\mathrm{S}}}\right) T_{\mathrm{eX}}} \tag{S12}$$

where $\aleph_{\mathrm{X}} = n_{\mathrm{X}} + ik_{\mathrm{X}}$ and $\aleph_{\mathrm{S}} = n_{\mathrm{S}} + ik_{\mathrm{S}}$ are the complex refractive indices of the lossy material and the substrate respectively, $T_{\mathrm{eX}} = \tan(dk_0\aleph_{\mathrm{X}})$ with $k_0 = 2\pi/\lambda$.

From the first and second partial derivatives of Eq. S12 with respect to $\omega$, and using $\aleph_{\mathrm{X}} = n_{\mathrm{X}}$, the condition for the minimum reflectance can be derived as [1]

$$\omega_d = \frac{1}{2d}\left[\frac{2m+1}{2n_{\mathrm{X}}(\omega_d)} - \frac{1}{2\pi n_{\mathrm{X}}(\omega_d)} tan^{-1}\left\{\frac{-2n_{\mathrm{X}}(\omega_d)k_s)}{n_{\mathrm{X}}(\omega_d)^2 - n_s^2 - k_s^2}\right\}\right] \tag{S13}$$

This is shown in Fig. S5a for a material following Lorentz dispersion with $\omega_{TO} = 1361\,\mathrm{cm}^{-1}$, $\omega_{LO} = 1635\,\mathrm{cm}^{-1}$, $\gamma = 8.75\,\mathrm{cm}^{-1}$ and $\epsilon_{inf} = 4.75$ (same as the parameters of hBN retrieved in this work) for different values of material thickness ($d$). We see that in the 1st order ($m = 0$), we have two possible dips, one close to material resonances ($\omega_d < \omega_{\mathrm{TO}}$) and other at higher frequencies far from the material resonances ( $\omega_d > \omega_{\mathrm{LO}}$). This is true if we have the material thickness larger than a cut off value (in Fig. S5 there are no dips for $d = 100\,\mathrm{nm}$). For this work, flake thicknesses were chosen such that the respective reflectance dips cover a broad range of wavelengths.

For the same material the reflectance was calculated analytically for two different thicknesses, while considering complex $\epsilon$ and also when only $Re\{\epsilon\}$ was considered. We see that though there is a large variation in $R$, however $\omega_d$ is negligibly affected by $Im\{\epsilon\}$. Hence, Eq. S13 can be applied for regions outside the RB of the material.

The FTIR microscope is equipped with two knife-edges to chose accurately the aperture defining the region of interest (ROI) of the spectral measurement. This is shown in Fig. S6. For each flake, the ROI for the spectral measurement was chosen such that the thickness is uniform in the ROI. The measured value of thickness in the respective ROI was used to calculate $n$ by Eq. S13. It should be noted that the signals have lower signal to noise ratio for smaller ROI and this results in lower precision in determining $\omega_d$ and hence $n$.

For determining $k$ in the Reststrahlen Band (RB), the expression for the reflection coefficient at $\Psi = 45°$ from Eq. S11 can be written as

$$2r(\omega, \Psi = 45°) = \frac{\left(1 - \frac{1}{\aleph_{\mathrm{S}}}\right) + i\left(\frac{1}{ik_{\mathrm{X}}} - \frac{ik_{\mathrm{X}}}{\aleph_{\mathrm{S}}}\right) T_{\mathrm{eX}}}{\left(1 + \frac{1}{\aleph_{\mathrm{S}}}\right) - i\left(\frac{1}{ik_{\mathrm{X}}} + \frac{ik_{\mathrm{X}}}{\aleph_{\mathrm{S}}}\right) T_{\mathrm{eX}}} + \frac{\left(1 - \frac{1}{\aleph_{\mathrm{S}}}\right) + i\left(\frac{1}{\aleph_{\mathrm{Y}}} - \frac{\aleph_{\mathrm{Y}}}{\aleph_{\mathrm{S}}}\right) T_{\mathrm{eY}}}{\left(1 + \frac{1}{\aleph_{\mathrm{S}}}\right) - i\left(\frac{1}{\aleph_{\mathrm{Y}}} + \frac{\aleph_{\mathrm{Y}}}{\aleph_{\mathrm{S}}}\right) T_{\mathrm{eY}}} \tag{S14}$$

where $T_{\mathrm{eX}} = \tan(idk_0k_{\mathrm{X}})$ and $T_{\mathrm{eY}} = \tan(dk_0\aleph_{\mathrm{Y}})$. Having predetermined $\aleph_{\mathrm{Y}} = n_{\mathrm{Y}} + ik_{\mathrm{Y}}$, the only unknown in Eq. S14 is $k_{\mathrm{X}}$. For each flake of thickness $d$, we calculate the frequency of the minimum of $R(\omega, \Psi = 45°) = |r(\omega, \Psi = 45°)|^2$ from Eq. S14 for different values of $k_{\mathrm{X}}$. Comparing this value of the dip position to the experimental $\omega_{\mathrm{d}}(k_{\mathrm{X}}, \Psi = 45°)$ we determine the value of $k_{\mathrm{X}}$.

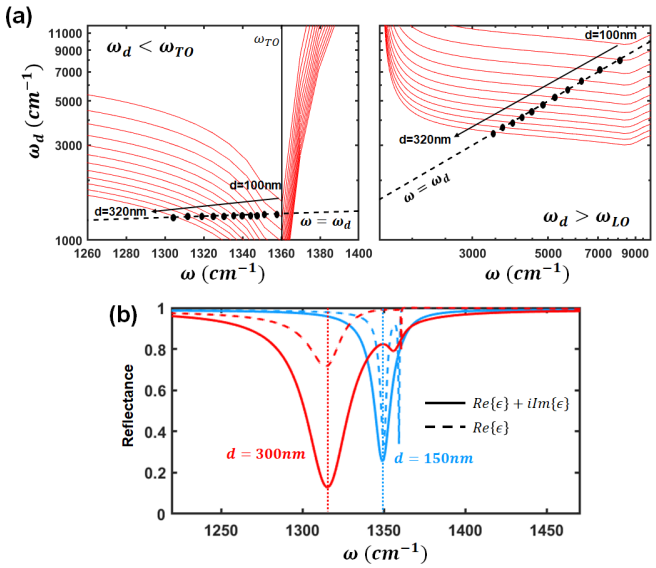


**Fig. S5** (a) Reflectance dip positions ($\omega_d$) as a function of incident frequency ($\omega$) for a polar material on a gold substrate according to Eq. S13. The material thickness is varied from $d = 100\,\text{nm}$ to $d = 320\,\text{nm}$ with steps of 20 nm.The expected positions of the reflectance dips for each $d$ are marked with black dots. (b) The reflectance calculated analytically for hBN with $d = 150\,\text{nm}$ and $d = 300\,\text{nm}$, for $\epsilon$ being complex (solid lines) or when $\epsilon$ is considered to be real (dashed lines).

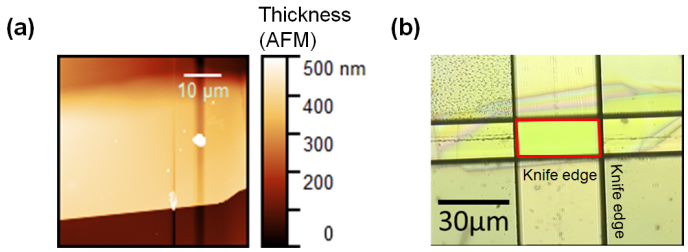


**Fig. S6** (a) The thickness of a hBN flake on gold substrate as measured by AFM. (b) FTIR microscope image of the same flake with the knife edges. The ROI chosen for the measurement is shown by the red box. The thickness of the flake in the ROI was 305 nm.

## 2.3 Experimental data for hBN

For hBN, 11 flakes (Fig. S3) were used to obtain the dips in spectral regions outside the RB. The experimental $\omega_\text{d}$ along with the evaluated $n$ are shown in Table S1. The same data points ($n$) are shown in Fig. 4d of the main article.

## 2.4 Experimental data for $\alpha$-$MoO_3$

To retrieve the permittivity of $\alpha$-$MoO_3$ along X, 13 flakes were used, resulting in 24 data points (11 in $\omega_\text{d} < \omega_\text{TO}$ and 13 in $\omega_\text{d} > \omega_\text{LO}$ spectral regions). The spectra are

**Table S1** Experimental results for hBN: 20 data points from the 11 flakes shown in Fig. S3.

| $d$ (nm) | $\omega_{\rm d}(<\omega_{\rm TO})\,{\rm cm}^{-1}$ | $n(\omega_{\rm d}<\omega_{\rm TO})$ | $\omega_{\rm d}(>\omega_{\rm LO})\,{\rm cm}^{-1}$ | $n(\omega_{\rm d}>\omega_{\rm LO})$ |
|---|---|---|---|---|
| 117±5 | 1355±1.8 | 13.19 | - | - |
| 125±5 | 1353±1.8 | 12.49 | - | - |
| 130±2 | 1354±1.8 | 12.08 | - | - |
| 133±2 | 1352±1.8 | 11.86 | - | - |
| 155±10 | 1350±1.8 | 10.40 | 6451± 42 | 2.18 |
| 160±10 | 1348±1.8 | 10.13 | 5682±32 | 2.41 |
| 165±3 † | 1349±1.8 | 9.87 | 5556±50 | 2.39 |
| 168±3 † | 1347±1.8 | 9.76 | 5618±52 | 2.34 |
| 220±15 | 1334±1.7 | 7.70 | 5025±55 | 2.05 |
| 285±5 | 1318±1.7 | 6.15 | 4124±47 | 1.97 |
| 305±10 | 1315±1.7 | 5.79 | 4032±46 | 1.89 |
| 320±10 | 1304±1.7 | 5.58 | 4000±46 | 1.82 |

†: denotes different positions of the same flake.

shown in Fig. S7 (red lines) and the data is tabulated in Table S2. The same data points are shown in Fig. 5d of the main article.

**Table S2** Experimental results for $\alpha$-$MoO_3$ to retrieve the permittivity along X: 24 data points from the 13 flakes shown in Fig. S7.

| $d$(nm) | $\omega_{\rm d}(<\omega_{\rm TO}){\rm cm}^{-1}$ | $n(\omega_{\rm d}<\omega_{\rm TO})$ | $\omega_{\rm d}(>\omega_{\rm LO}){\rm cm}^{-1}$ | $n(\omega_{\rm d}>\omega_{\rm LO})$ |
|---|---|---|---|---|
| 350±10 | 806.5±3.3 | 8.29 | 3333± 60 | 2.01 |
| 480±10 | 788.6±3.1 | 6.29 | 2500± 60 | 2.03 |
| 484±10 | 788.0±3.1 | 6.24 | 2439± 60 | 1.97 |
| 550±10 | 784.9±3.1 | 5.54 | 2174± 55 | 2.00 |
| 566±10 | 770.4±3.0 | 5.50 | 2083± 55 | 2.03 |
| 920±15 | 716.8±1.6 | 3.69 | 1408±50 | 1.88 |
| 1100±30 | 685.9±2.1 | 3.24 | 1329±50 | 1.67 |
| 1200±30 | 666.7±2.2 | 3.06 | 1282±44 | 1.59 |
| 1425±50 | 627.4±2.0 | 2.74 | 1205±42 | 1.43 |
| 1429±50 | 620.3±2.0 | 2.77 | 1124±60 | 1.53 |
| 1500±50 | 613.5±2.0 | 2.67 | 1136±32 | 1.44 |
| 1800±50 | - | - | 1111±32 | 1.23 |
| 2200±50 | - | - | 1036±30 | 1.08 |

For the permittivity along Y, we used 9 of the 13 flakes shown in Fig. S7, to get $n_{\rm Y}$ in the spectral region $\omega>\omega_{\rm LO}$. The $k_{\rm Y}$ was retrieved from 5 of the same 13 flakes. The data points are shown in Fig. 6b,c of the main article and tabulated in Table S3.

**Table S3** Experimental results for $\alpha$-$MoO_3$ to retrieve the permittivity along Y: 14 data points from the 10 flakes shown in Fig. S7.

| $d$ (nm) | $\omega_{\rm d}(>\omega_{\rm LO})$ cm$^{-1}$ | $n(\omega_{\rm d}>\omega_{\rm LO})$ | $\omega_{\rm d,RB}$ cm$^{-1}$ | $k(\omega_{\rm d,RB})$ |
|---|---|---|---|---|
| 350±10 | 3175±60 | 2.11 | - | - |
| 480±10 | 2381±60 | 2.08 | - | - |
| 484±10 | 2222±60 | 2.21 | - | - |
| 550±10 | 2160±55 | 2.01 | - | - |
| 566±10 | 2083±55 | 2.03 | - | - |
| 920±15 | 1370±50 | 1.93 | 727.3±1.5 | 2.0 |
| 1100±30 | - | - | 693.5±2.1 | 2.6 |
| 1200±30 | 1299±44 | 1.57 | 674.8±2.1 | 2.86 |
| 1429±50 | 1053±60 | 1.63 | 641.0±1.9 | 3.34 |
| 1500±50 | 1111±40 | 1.47 | 633.7±2.0 | 3.88 |

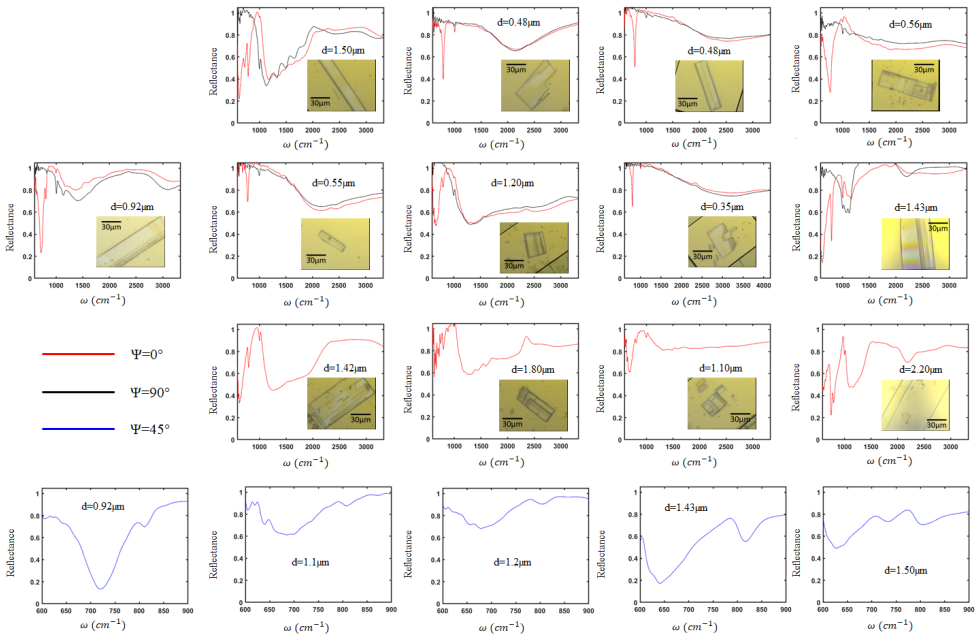


**Fig. S7** The experimental reflectance spectra for each of the 13 $\alpha$-$MoO_3$ flakes as obtained by the FTIR when the incident light is polarized along X (red) and along Y (black). The microscope images of the corresponding flakes are shown as inset along with the thickness of the flake as measured by AFM.

## 3 Uncertainty on permittivity estimations.

Separating the real and imaginary parts of the permittivity given by Eq. 1, we write it as $\epsilon = \epsilon_{\mathrm{rs}} + i\epsilon_{\mathrm{is}}$ where

$$\begin{aligned}\epsilon_{\mathrm{rs}} &= \epsilon_{\mathrm{inf}}\left[1 + \frac{(\omega_{\mathrm{LO}}^2 - \omega_{\mathrm{TO}}^2)(\omega_{\mathrm{TO}}^2 - \omega^2)}{(\omega_{\mathrm{TO}}^2 - \omega^2)^2 + (\omega\gamma)^2}\right] \\ \epsilon_{\mathrm{is}} &= \epsilon_{\mathrm{inf}}\frac{\omega\gamma(\omega_{\mathrm{LO}}^2 - \omega_{\mathrm{TO}}^2)}{(\omega_{\mathrm{TO}}^2 - \omega^2)^2 + (\omega\gamma)^2}\end{aligned} \tag{S15}$$

The partial derivatives of $\epsilon_{\mathrm{r}}$ with respect to the four dielectric parameters are

$$\begin{aligned}\frac{\partial\epsilon_{\mathrm{rs}}}{\partial\epsilon_{\mathrm{inf}}} &= \left[1 + \frac{(\omega_{\mathrm{LO}}^2 - \omega_{\mathrm{TO}}^2)(\omega_{\mathrm{TO}}^2 - \omega^2)}{(\omega_{\mathrm{TO}}^2 - \omega^2)^2 + (\omega\gamma)^2}\right] \\ \frac{\partial\epsilon_{\mathrm{rs}}}{\partial\omega_{\mathrm{TO}}} &= \epsilon_{\mathrm{inf}}\frac{2\omega_{\mathrm{TO}}\left(\omega^2\gamma^2(\omega_{\mathrm{LO}}^2 + \omega^2 - 2\omega_{\mathrm{TO}}^2) - (\omega_{\mathrm{LO}}^2 - \omega^2)(\omega_{\mathrm{TO}}^2 - \omega^2)^2\right)}{\left((\omega_{\mathrm{TO}}^2 - \omega^2)^2 + (\omega\gamma)^2\right)^2} \\ \frac{\partial\epsilon_{\mathrm{rs}}}{\partial\omega_{\mathrm{LO}}} &= \epsilon_{\mathrm{inf}}\frac{2\omega_{\mathrm{LO}}(\omega_{\mathrm{TO}}^2 - \omega^2)}{(\omega_{\mathrm{TO}}^2 - \omega^2)^2 + (\omega\gamma)^2} \\ \frac{\partial\epsilon_{\mathrm{rs}}}{\partial\gamma} &= \epsilon_{\mathrm{inf}}\frac{2\omega^2\gamma(\omega_{\mathrm{LO}}^2 - \omega_{\mathrm{TO}}^2)(\omega_{\mathrm{TO}}^2 - \omega^2)}{\left((\omega_{\mathrm{TO}}^2 - \omega^2)^2 + (\omega\gamma)^2\right)^2}\end{aligned} \tag{S16}$$

The same for $\epsilon_{\mathrm{is}}$ are

$$\begin{aligned}\frac{\partial\epsilon_{\mathrm{is}}}{\partial\epsilon_{\mathrm{inf}}} &= \frac{\omega\gamma(\omega_{\mathrm{LO}}^2 - \omega_{\mathrm{TO}}^2)}{(\omega_{\mathrm{TO}}^2 - \omega^2)^2 + (\omega\gamma)^2} \\ \frac{\partial\epsilon_{\mathrm{is}}}{\partial\omega_{\mathrm{TO}}} &= -\epsilon_{\mathrm{inf}}\frac{2\gamma\omega\omega_{\mathrm{TO}}\left(\omega^2\gamma^2 - (\omega_{\mathrm{TO}}^2 - \omega^2)^2(\omega_{\mathrm{TO}}^2 + \omega^2 - 2\omega_{\mathrm{LO}}^2)\right)}{\left((\omega_{\mathrm{TO}}^2 - \omega^2)^2 + (\omega\gamma)^2\right)^2} \\ \frac{\partial\epsilon_{\mathrm{is}}}{\partial\omega_{\mathrm{LO}}} &= \epsilon_{\mathrm{inf}}\frac{2\omega_{\mathrm{LO}}\omega\gamma}{(\omega_{\mathrm{TO}}^2 - \omega^2)^2 + (\omega\gamma)^2} \\ \frac{\partial\epsilon_{\mathrm{is}}}{\partial\gamma} &= \epsilon_{\mathrm{inf}}\frac{\omega(\omega_{\mathrm{LO}}^2 - \omega_{\mathrm{TO}}^2)\left((\omega_{\mathrm{TO}}^2 - \omega^2)^2 - \omega^2\gamma^2\right)}{\left((\omega_{\mathrm{TO}}^2 - \omega^2)^2 + (\omega\gamma)^2\right)^2}\end{aligned} \tag{S17}$$

With the standard errors on the four dielectric permittivities being $\sigma_{\epsilon_{\mathrm{inf}}}$, $\sigma_{\omega_{\mathrm{TO}}}$, $\sigma_{\omega_{\mathrm{LO}}}$, $\sigma_\gamma$, the total uncertainty on permittivity estimation for the real and imaginary

parts respectively, is then given as

$$\begin{aligned}
\sigma^2_{\epsilon_{\mathrm{rs}}} &= \left(\frac{\partial \epsilon_{\mathrm{rs}}}{\partial \epsilon_{\mathrm{inf}}}\right)^2 \sigma^2_{\epsilon_{\mathrm{inf}}} + \left(\frac{\partial \epsilon_{\mathrm{rs}}}{\partial \omega_{\mathrm{TO}}}\right)^2 \sigma^2_{\omega_{\mathrm{TO}}} + \left(\frac{\partial \epsilon_{\mathrm{rs}}}{\partial \omega_{\mathrm{LO}}}\right)^2 \sigma^2_{\omega_{\mathrm{LO}}} + \left(\frac{\partial \epsilon_{\mathrm{rs}}}{\partial \gamma}\right)^2 \sigma^2_{\gamma} \\
\sigma^2_{\epsilon_{\mathrm{is}}} &= \left(\frac{\partial \epsilon_{\mathrm{is}}}{\partial \epsilon_{\mathrm{inf}}}\right)^2 \sigma^2_{\epsilon_{\mathrm{inf}}} + \left(\frac{\partial \epsilon_{\mathrm{is}}}{\partial \omega_{\mathrm{TO}}}\right)^2 \sigma^2_{\omega_{\mathrm{TO}}} + \left(\frac{\partial \epsilon_{\mathrm{is}}}{\partial \omega_{\mathrm{LO}}}\right)^2 \sigma^2_{\omega_{\mathrm{LO}}} + \left(\frac{\partial \epsilon_{\mathrm{is}}}{\partial \gamma}\right)^2 \sigma^2_{\gamma}
\end{aligned} \tag{S18}$$

when only a single oscillator is considered as in the case of hBN or along the Y direction of $\alpha$-$MoO_3$.

When two oscillators are involved like in the case of the X direction of $\alpha$-$MoO_3$, we write the permittivity as $\epsilon = \epsilon_{\mathrm{r}} + i\epsilon_{\mathrm{i}} = \epsilon_{\mathrm{inf}}(\epsilon_{\mathrm{r}_1} + i\epsilon_{\mathrm{i}_1})(\epsilon_{\mathrm{r}_2} + i\epsilon_{\mathrm{i}_2})$ where

$$\begin{aligned}
\epsilon_{\mathrm{r_u}} &= 1 + \frac{(\omega^2_{\mathrm{LO_u}} - \omega^2_{\mathrm{TO_u}})(\omega^2_{\mathrm{TO_u}} - \omega^2)}{(\omega^2_{\mathrm{TO_u}} - \omega^2)^2 + (\omega\gamma_{\mathrm{u}})^2} \\
\epsilon_{\mathrm{i_u}} &= \epsilon_{\mathrm{inf}} \frac{\omega\gamma_{\mathrm{l}}(\omega^2_{\mathrm{LO_u}} - \omega^2_{\mathrm{TO_u}})}{(\omega^2_{\mathrm{TO_u}} - \omega^2)^2 + (\omega\gamma_{\mathrm{u}})^2}
\end{aligned} \tag{S19}$$

with u=1,2, the index of the oscillators. Then the partial derivatives with respect to the dielectric parameters $\mathcal{P}_{\mathrm{u}}$=$\omega_{\mathrm{TO_u}}$, $\omega_{\mathrm{LO_u}}$,$\gamma_{\mathrm{u}}$ and $\epsilon_{\mathrm{inf}}$ are then written as

$$\begin{aligned}
\frac{\partial \epsilon_{\mathrm{r_u}}}{\partial \mathcal{P}_{\mathrm{u}}} &= \frac{1}{\epsilon_{\mathrm{inf}}} \frac{\partial \epsilon_{\mathrm{rs}}}{\partial \mathcal{P}_{\mathrm{u}}} \qquad \frac{\partial \epsilon_{\mathrm{i_u}}}{\partial \mathcal{P}_{\mathrm{u}}} = \frac{1}{\epsilon_{\mathrm{inf}}} \frac{\partial \epsilon_{\mathrm{is}}}{\partial \mathcal{P}_{\mathrm{u}}} \\
\frac{\partial \epsilon_{\mathrm{r_u}}}{\partial \epsilon_{\mathrm{inf}}} &= \frac{\partial \epsilon_{\mathrm{rs}}}{\partial \epsilon_{\mathrm{inf}}} \qquad \frac{\partial \epsilon_{\mathrm{i_u}}}{\partial \epsilon_{\mathrm{inf}}} = \frac{\partial \epsilon_{\mathrm{is}}}{\partial \epsilon_{\mathrm{inf}}}
\end{aligned} \tag{S20}$$

The partial derivatives of $\epsilon_{\mathrm{rs}}$ and $\epsilon_{\mathrm{is}}$ are given by Eq. S16 and Eq. S17. The partial derivatives of $\epsilon_{\mathrm{r}}$ and $\epsilon_{\mathrm{i}}$ with respect to the parameters $\mathcal{P}_{\mathrm{u}}$ and $\epsilon_{\mathrm{inf}}$ can then be written as

$$\begin{aligned}
\frac{\partial \epsilon_{\mathrm{r}}}{\partial \mathcal{P}_{\mathrm{u}}} &= \epsilon_{\mathrm{inf}} \left[\frac{\partial \epsilon_{\mathrm{r_u}}}{\partial \mathcal{P}_{\mathrm{u}}} \epsilon_{\mathrm{r_v}} - \frac{\partial \epsilon_{\mathrm{i_u}}}{\partial \mathcal{P}_{\mathrm{u}}} \epsilon_{\mathrm{i_v}}\right] \\
\frac{\partial \epsilon_{\mathrm{i}}}{\partial \mathcal{P}_{\mathrm{u}}} &= \epsilon_{\mathrm{inf}} \left[\frac{\partial \epsilon_{\mathrm{i_u}}}{\partial \mathcal{P}_{\mathrm{u}}} \epsilon_{\mathrm{r_v}} + \frac{\partial \epsilon_{\mathrm{r_u}}}{\partial \mathcal{P}_{\mathrm{u}}} \epsilon_{\mathrm{i_v}}\right] \\
\frac{\partial \epsilon_{\mathrm{r}}}{\partial \epsilon_{\mathrm{inf}}} &= \epsilon_{\mathrm{r_u}} \epsilon_{\mathrm{r_v}} - \epsilon_{\mathrm{i_u}} \epsilon_{\mathrm{i_v}} \\
\frac{\partial \epsilon_{\mathrm{i}}}{\partial \epsilon_{\mathrm{inf}}} &= \epsilon_{\mathrm{i_u}} \epsilon_{\mathrm{r_v}} + \epsilon_{\mathrm{i_v}} \epsilon_{\mathrm{r_u}}
\end{aligned} \tag{S21}$$

with v being the index of the oscillators and v≠u. The total uncertainty on the estimation of $\epsilon$ ($\sigma_{\epsilon_r}$ and $\sigma_{\epsilon_i}$) for the case of two oscillators, can then be calculated using Eq. S18, considering the standard errors and partial derivatives with respect to all the dielectric parameters involved.

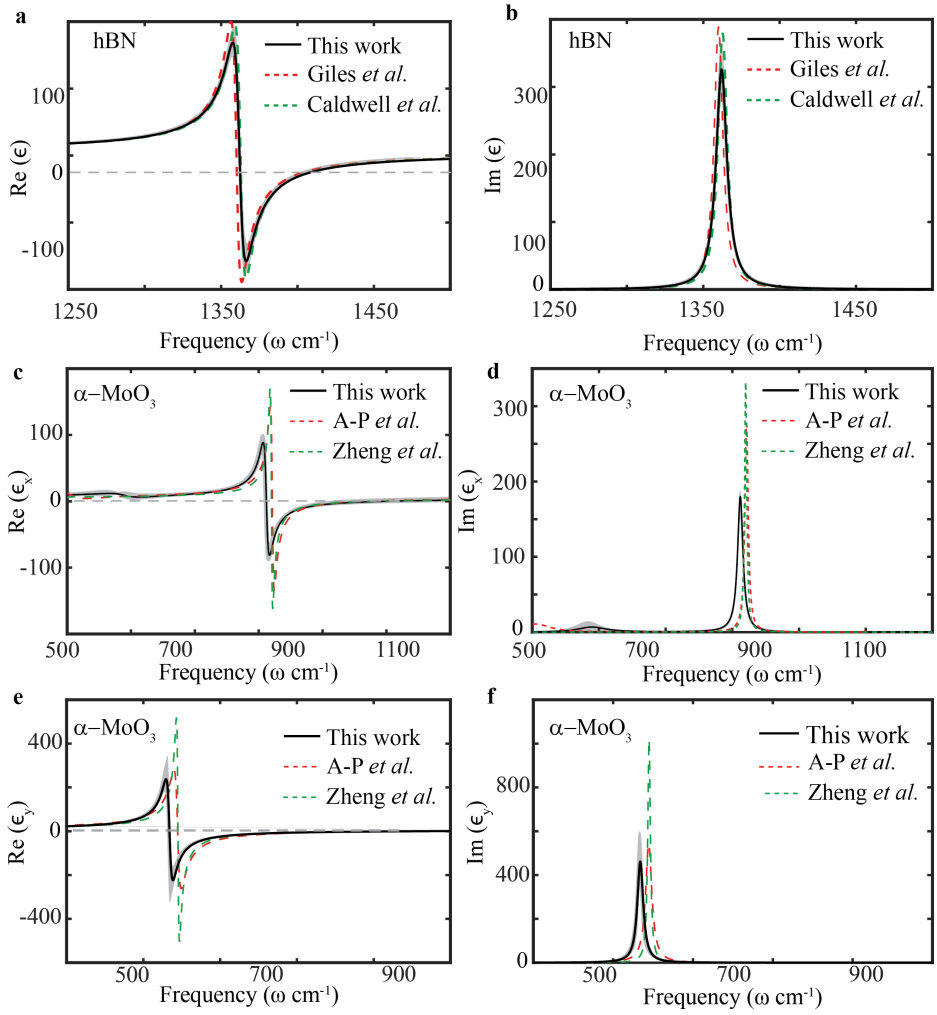


**Fig. S8 Comparing the extracted dielectric function with previous reports.** (a,b) Real and imaginary parts of the dielectric function $\epsilon(\omega)$ for hBN extracted by our method and those reported by Giles *et al.* [2] and Caldwell *et al.* [3]. (c–f) The same for $\alpha$-$MoO_3$ along x and y. Extracted values are compared with literature data from Alvarez-Pérez *et al.* [4] and Zheng *et al.* [5]; for all panels, the uncertainties are shaded in gray.

# References


[1] Park, K.C.: The Extreme Values of Reflectivity and the Conditions for Zero Reflection from Thin Dielectric Films on Metal. Applied Optics **3**(7), 877–881 (1964) https://doi.org/10.1364/AO.3.000877

[2] Giles, A.J., Dai, S., Vurgaftman, I., Hoffman, T., Liu, S., Lindsay, L., Ellis, C.T., Assefa, N., Chatzakis, I., Reinecke, T.L., Tischler, J.G., Fogler, M.M., Edgar, J.H., Basov, D.N., Caldwell, J.D.: Ultralow-loss polaritons in isotopically pure boron nitride. Nature Materials **17**(2), 134–139 (2018) https://doi.org/10.1038/nmat5047

[3] Caldwell, J.D., Kretinin, A.V., Chen, Y., Giannini, V., Fogler, M.M., Francescato, Y., Ellis, C.T., Tischler, J.G., Woods, C.R., Giles, A.J., Hong, M., Watanabe, K., Taniguchi, T., Maier, S.A., Novoselov, K.S.: Sub-diffractional volume-confined polaritons in the natural hyperbolic material hexagonal boron nitride. Nature Communications **5**(1), 5221 (2014) https://doi.org/10.1038/ncomms6221

[4] Álvarez-Pérez, G., Folland, T.G., Errea, I., Taboada-Gutiérrez, J., Duan, J., Martín-Sánchez, J., Tresguerres-Mata, A.I.F., Matson, J.R., Bylinkin, A., He, M., Ma, W., Bao, Q., Martín, J.I., Caldwell, J.D., Nikitin, A.Y., Alonso-González, P.: Infrared Permittivity of the Biaxial van der Waals Semiconductor $\alpha$-MoO3 from Near- and Far-Field Correlative Studies. Advanced Materials **32**(29), 1908176 (2020) https://doi.org/10.1002/adma.201908176

[5] Zheng, Z., Xu, N., Oscurato, S.L., Tamagnone, M., Sun, F., Jiang, Y., Ke, Y., Chen, J., Huang, W., Wilson, W.L., Ambrosio, A., Deng, S., Chen, H.: A mid-infrared biaxial hyperbolic van der Waals crystal. Science Advances **5**(5), 8690 (2019) https://doi.org/10.1126/sciadv.aav8690